



1 **Iron “Ore” Nothing: Benthic iron fluxes from the oxygen-deficient Santa Barbara Basin**
2 **enhance phytoplankton productivity in surface waters**

3

4 **De’Marcus Robinson^{1*}, Anh L.D. Pham¹, David J. Yousavich², Felix Janssen³, Frank**
5 **Wenzhöfer³, Eleanor C. Arrington⁴, Kelsey M. Gosselin⁵, Marco Sandoval-Belmar¹,**
6 **Matthew Mar¹, David L. Valentine⁴, Daniele Bianchi¹, Tina Treude^{1,2*}**

7

8 ¹Department of Atmospheric and Oceanic Sciences, University of California Los Angeles, Los
9 Angeles, CA, USA

10 ²Department of Earth, Planetary, and Space Sciences, University of California Los Angeles, Los
11 Angeles, CA, USA

12 ³HGF-MPG Joint Research Group for Deep-Sea Ecology and Technology, Alfred Wegener
13 Institute, Helmholtz Centre for Polar and Marine Research, Bremerhaven, Germany

14 ⁴Department of Earth Science and Marine Science Institute, University of California, Santa
15 Barbara, CA 93106, USA

16 ⁵Interepartment Graduate Program in Marine Science, University of California, Santa Barbara, CA
17 93106, USA

18

19 *Correspondence: De’Marcus Robinson, demarcus1.robinson@atmos.ucla.edu; Tina Treude,
20 ttreude@g.ucla.edu

21

22



23 **Abstract**

24

25 The trace metal iron (Fe) is an essential micronutrient that controls phytoplankton productivity,
26 which subsequently affects the cycling of macronutrients. Along the continental margin of the U.S.
27 West Coast, high benthic Fe release has been documented, in particular from deep anoxic basins
28 in the Southern California Borderland. However, the influence of this Fe release on surface
29 primary production remains poorly understood. In the present study from the Santa Barbara Basin,
30 in-situ benthic Fe fluxes were determined along a transect from shallow to deep sites in the basin.
31 Fluxes ranged between 0.23 and 4.9 mmol m⁻² d⁻¹, representing some of the highest benthic Fe
32 fluxes reported to date. To investigate the influence of benthic Fe release from the oxygen-deficient
33 deep basin on surface phytoplankton production, we combined benthic flux measurements with
34 numerical simulations using the Regional Ocean Model System coupled to the Biogeochemical
35 Elemental Cycling model (ROMS-BEC). For this purpose, we updated existing Fe flux
36 parameterization to include new benthic fluxes from the Santa Barbara Basin. Our simulation
37 suggests benthic iron fluxes support surface primary production creating positive feedback on
38 benthic Fe release by enhancing low oxygen conditions in bottom waters. However, the easing of
39 phytoplankton Fe limitation near the coast may be partially compensated by increased nitrogen
40 limitation further offshore, reducing the efficacy of this positive feedback.

41



42 1. Introduction

43 The California Current System (CCS), located off the coasts of Washington, Oregon, and
44 California, is a typical Eastern Boundary Upwelling System, where seasonal upwelling supports a
45 highly diverse and productive marine ecosystem (Chavez and Messié, 2009; Carr and Kearns,
46 2003). The CCS can be split into three main parts: the main equatorward California Current
47 offshore, a subsurface poleward undercurrent fringing the continental shelf, and a recirculation
48 pattern known as the Southern California Eddy in the Southern California Bight.

49 In the CCS, both upwelling and large-scale circulation provide essential nutrients to the euphotic
50 zone, where they fuel high rates of net primary production (NPP). While seasonal upwelling
51 dominates north of Point Conception, advection by the CCS provides a major route for nutrient
52 supply to the Santa Barbara Channel in the Southern California Bight (Bray et al., 1999). Following
53 phytoplankton blooms, sinking and degradation of organic matter lead to oxygen consumption and
54 widespread oxygen loss in subsurface waters (Brander et al., 2017; Chavez and Messié, 2009).
55 Along the southern California coast, this oxygen depletion is exacerbated by regional circulation
56 patterns that include transport of low-oxygen waters of tropical origin along the poleward
57 undercurrent (Evans et al., 2020; Pozo Buil and Di Lorenzo, 2017). Oxygen decline is particularly
58 apparent in deep, isolated basins such as those found in the Southern California continental
59 borderland, where the presence of shallow sills limits ventilation of deep waters and anoxic
60 conditions are often encountered near the bottom (Reimers et al., 1990; Goericke et al., 2015;
61 White et al., 2019).

62 In the CCS, the trace metal iron (Fe) has been identified as a limiting factor for the growth of
63 phytoplankton (Hogle et al., 2018). Fe is an essential micronutrient that has also a considerable
64 influence on the dynamics of phosphorus and nitrogen in the euphotic zone (Tagliabue et al., 2017).
65 Similar to other nutrients, Fe is transported to the surface by upwelling and circulation, but the
66 supply is generally low in an oxic environment relative to other macronutrients, reflecting rapid
67 scavenging of the insoluble iron-oxide minerals by sinking particles that eventually accumulate in
68 the sediment (Bruland et al., 2001, 2014; Firme et al., 2003; Till et al., 2019). While early studies
69 suggested that Fe inputs to the CCS are dominated by rivers and aeolian deposition (Biller and
70 Bruland, 2013; Johnson et al., 2003), more recent work highlights a combination of sources,



71 including benthic fluxes (Severmann et al., 2010; Noffke et al., 2012; Tagliabue et al., 2017) and
72 ocean currents, in redistributing Fe in coastal waters (Bray et al., 1999; Boiteau et al., 2019; García-
73 Reyes and Largier, 2010).

74 Importantly, benthic release of Fe(II), the reduced and soluble form of Fe, has been recognized as
75 a potential source of Fe to the surface ocean along the continental shelf and slope of the CCS,
76 including the deep basins of the California borderland (John et al., 2012; Severmann et al., 2010).
77 Under hypoxic or anoxic bottom water conditions, Fe(II) produced in the sediment during
78 microbial organic matter degradation coupled to Fe (III) reduction diffuses across the sediment-
79 water interface and accumulates in the water column (Furrer and Wehrli, 1993; Dale et al., 2015;
80 Severmann et al., 2010). In the CCS, this benthic Fe flux is likely to exceed atmospheric deposition
81 (Deutsch et al., 2021a), and may ultimately make its way to the surface by upwelling and vertical
82 mixing, supporting high rates of photosynthesis.

83 The interaction between low bottom water oxygen, Fe(II) release, and transport by the ocean
84 circulation are particularly important in the Santa Barbara Basin (SBB), an oxygen-deficient basin
85 located between the Channel Islands and mainland California in the Southern California Bight.
86 The SBB frequently experiences seasonal anoxia in the bottom water in fall, with irregular oxygen
87 flushing of dense, hypoxic water below the western sill depth (470 m) during winter and spring
88 (Goericke et al., 2015; Sholkovitz and Soutar, 1975; White et al., 2019). This seasonal flushing
89 reflects either changes in upwelling strength and frequency, or changes in stratification at the sill
90 depth, although the exact cause of the flushing is still unclear (Goericke et al., 2015; Sholkovitz
91 and Gieskes, 1971; White et al., 2019). Lack of oxygen in the deeper parts of the basin support
92 anaerobic microbial processes in the bottom water and sediment (White et al., 2019), including
93 benthic Fe reduction (Goericke et al., 2015) causing the release of Fe(II) into the water column
94 (Severmann et al., 2010). Ventilation events that re-oxygenate the deep basin, as well as mixing
95 by the vigorous submesoscale circulation (Kessouri et al., 2020) could allow upwelling of this Fe
96 above the sill depth and ultimately to the surface, providing a linkage between benthic processes
97 and upper water column biogeochemistry. Increased surface primary production supported by this
98 Fe source would in turn drive higher remineralization and oxygen loss in deep waters, thus
99 providing positive feedback to benthic Fe release. However, with a dearth of benthic Fe flux
100 measurements in the SBB, gaps remain in our understanding of the dynamics and impact of benthic



101 Fe flux, particularly with respect to its magnitude, dependence on bottom water oxygen, and ability
102 to reach the euphotic zone and influence primary production.

103 In this study, we explore the connection between benthic Fe and surface primary production in the
104 CCS, by investigating the influence of enhanced benthic Fe fluxes from low-oxygen waters with
105 a combination of field observations and model experiments. We focus on the SBB, where we
106 provide a new set of benthic Fe flux data determined by in-situ benthic flux chamber
107 measurements. We combine these new observations with existing data (Severmann et al., 2010) to
108 revise the representation of benthic Fe fluxes in UCLA's Regional Ocean Modeling System
109 coupled to the Biogeochemical Elemental Cycling (ROMS-BEC) model (Deutsch et al., 2021a).
110 We use the model to evaluate the effect of benthic Fe fluxes on surface nutrient consumption and
111 NPP, and compare their impact to that of aeolian Fe deposition in the SBB and beyond.

112

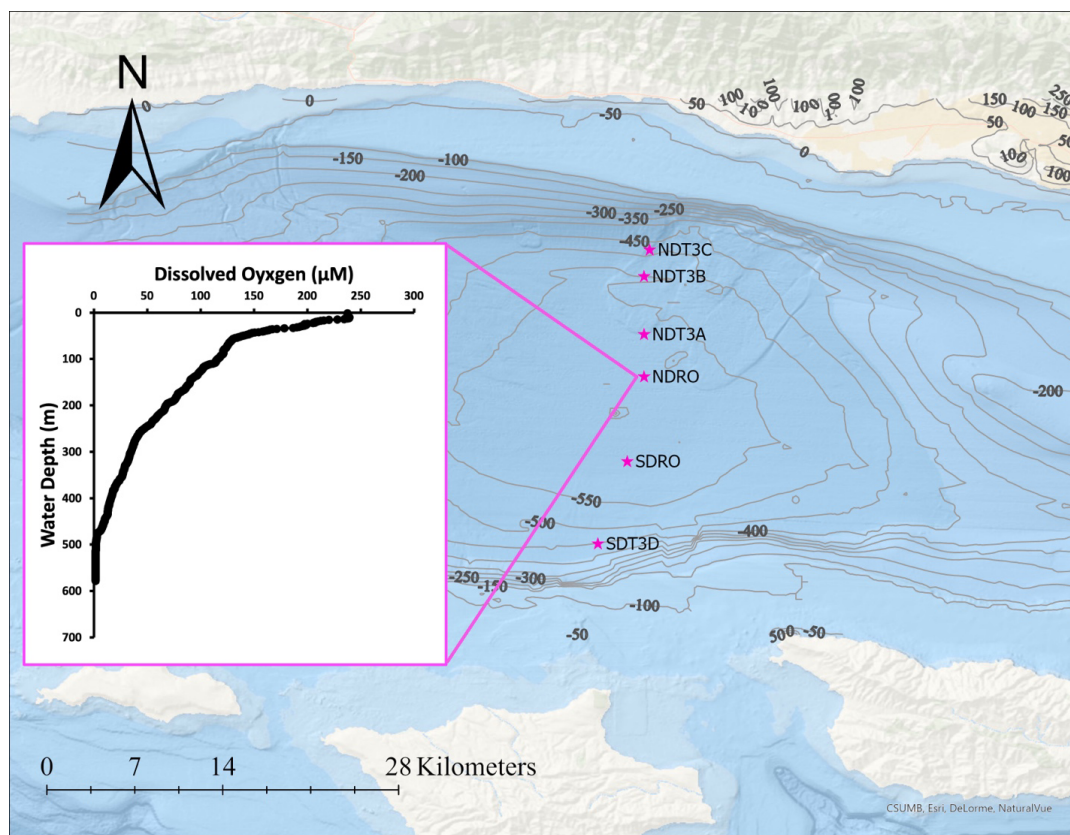


113 **2. Materials and Methods**

114 **2.1 Study Site**

115 Fieldwork in the SBB was accomplished between Oct 29 and Nov 11, 2019, during the R/V
116 Atlantis cruise AT42-19. Sampling occurred during the anoxic, non-upwelling season along one
117 bimodal transects with six stations total at depths between 447 and 585 m (**Fig. 1, Table 1**). The
118 map in **Fig. 1** was created using ArcGIS Ocean Basemap. The GEBCO bathymetric data source
119 was used to add contour lines.

120



121

122 **Figure 1.** Station locations in the SBB during the AT42-19 expedition with R/V Atlantis. NDT3
123 (with stations A, B, C) = North Depocenter Transect Three, NDRO = North Depocenter Radial
124 Origin, SDRO = Southern Depocenter Radial Origin, SDT3 (with station D) = Southern



125 Depocenter Transect Three. The small insert figure displays dissolved oxygen concentrations in
126 the water column at the NDRO station profiled by an optode sensor attached to the AUV Sentry.
127 The profile was measured at the following position: Latitude 34.2618, Longitude -120.0309.

128 Transects were divided into northern (NDT3 = North Depocenter Transect Three) and southern
129 (SDT3 = South Depocenter Transect Three) sites based on basin geography (**Fig. 1**). Stations were
130 labeled alphabetically from A (deepest) to D (shallowest) according to their location along the
131 transect, except for the deepest stations at the bottom of the basin, which were labeled Northern
132 Depocenter Radial Origin (NDRO) and Southern Depocenter Radial Origin (SDRO).

133 **2.2 Benthic Flux Chambers**

134 Custom-built cylindrical benthic flux chambers (Treude et al., 2009) were deployed by the ROV
135 Jason at the indicated stations (**Fig. 1**). Chambers were installed in a small lightweight frame made
136 from fiber-reinforced plastics. A stirrer was used to keep the water overlying the sediment enclosed
137 by the chamber well mixed. One or two replicate chambers were deployed at each site. Since
138 sediment in the SBB is quite soft and poorly consolidated, especially towards the deeper stations,
139 frames were fitted with platforms attached to the feet of the frame and with buoyant syntactic foam
140 to reduce sinking into the sediment. A syringe sampler equipped with 6 glass sampling syringes
141 withdrew 50 mL of the overlying seawater at pre-programmed times. A seventh syringe was used
142 to inject 50 mL of de-ionized water shortly after chambers were deployed to calculate chamber
143 volume from the salinity-drop recorded with a conductivity sensor (type 5860, Aanderaa Data
144 Instruments, Bergen, NO) in the overlying water, following the approach described in (Kononets
145 et al., 2021). Water samples were analyzed for Fe(II) on the ship using a Shimadzu UV-
146 Spectrophotometer (UV-1800), equipped with a sipper unit, following the procedure of (Grasshoff
147 and Ehrhardt, 1999). Fe fluxes were calculated from the slope of linear fits of Fe concentration
148 time series vs. time (**Fig. S1**), multiplied by the chamber volume, and divided by the surface area
149 of the sediment (Kononets et al., 2021).

150 **2.3 Numerical model (ROMS-BEC)**

151 To explore the impacts of benthic Fe fluxes on surface primary production, we used a well-
152 established ocean biogeochemical model of the CCS (Renault et al., 2016; Deutsch et al., 2021a).



153 The physical model component consists of the Regional Ocean Modeling System (ROMS),
154 (Shchepetkin, 2015; Shchepetkin and McWilliams, 2005) a primitive-equation, hydrostatic,
155 topography-following ocean model. As in prior work, the model domain spans the entire U.S. West
156 Coast, from Baja California to Vancouver Island, with a horizontal resolution of 4 km, enough to
157 resolve the mesoscale circulation (Capet et al., 2008). The baseline model configuration was run
158 over the period 1995–2017 with interannually varying atmospheric forcings. We refer the reader
159 to earlier publications (Renault et al., 2021; Deutsch et al., 2021a) for a complete description of
160 the model configuration, setup, forcings and boundary conditions used in this study.

161 ROMS is coupled online to the Biogeochemical Elemental Cycling (BEC) model (Moore et al.,
162 2004), adapted for the U.S. West Coast by (Deutsch et al., 2021b). BEC solves the equations for
163 the evolution of six nutrients (nitrate (NO_3^-), ammonium (NH_4^+), nitrite (NO_2^-), silicate (SiO_2),
164 phosphate (PO_4^{3-}), and iron (Fe)), three phytoplankton groups (small phytoplankton, diatoms, and
165 diazotrophs), a single zooplankton group, inorganic carbon, oxygen, and dissolved organic matter
166 (carbon, nitrogen, phosphorus, and iron). Nutrient and carbon cycles are coupled by a fixed
167 stoichiometry, except for silica and Fe, which use variable stoichiometries (Deutsch et al., 2021a;
168 Moore et al., 2001, 2004). The Fe cycle in BEC includes four separate pools: dissolved inorganic
169 Fe (dFe), dissolved and particulate organic Fe, and Fe associated with mineral dust. Of these, only
170 dissolved organic and inorganic Fe are explicitly tracked as state variables, while particulate Fe is
171 treated implicitly by resolving vertical sinking particle fluxes (Moore et al., 2001; Moore and
172 Braucher, 2008). Four main processes control the cycle of Fe: atmospheric deposition, biological
173 uptake and remineralization, scavenging by sinking particles, and release by sediment. The
174 atmospheric dFe deposition is based on the dust climatology of (Mahowald et al., 2006), and
175 dissolution rates from (Moore and Braucher, 2008). The benthic dFe flux is based on a compilation
176 of benthic flux chamber measurements on the California margin (Severmann et al., 2010) and is
177 parameterized as a function of the bottom water O_2 concentration, as discussed in (Deutsch et al.,
178 2021b) (see also Section 2.5). An Fe scavenging scheme removes dFe from the water column at a
179 rate proportional to sinking particle fluxes and dFe concentrations, assuming a uniform
180 concentration of 0.6 nM of Fe-binding ligands (Moore et al., 2004; Moore and Braucher, 2008).
181 Accordingly, scavenging rates increase rapidly at dFe concentrations greater than 0.6 nM, and
182 decreases rapidly below 0.5 nM (**Fig. S2**). Note that, while simplistic, this formulation is still
183 widely adopted by global ocean biogeochemistry models (Tagliabue et al., 2014, 2016), although



184 improvements have been proposed (Moore and Braucher, 2008; Aumont et al., 2015; Pham and
185 Ito, 2019, 2018).

186 As shown in previous work, the model captures the main patterns of physical and biogeochemical
187 variability in the CCS, providing a representation of nutrient cycles and NPP in good agreement
188 with observations (Renault et al., 2021; Deutsch et al., 2021b). In this paper, we further evaluate
189 the model solution against an extended set of dissolved Fe measurements for the CCS (see Sections
190 **2.4** and **3.1**).

191 **2.4 Fe dataset along the U.S. West Coast**

192 For evaluating the model ability to capture observed patterns in dFe, we compiled a dataset of the
193 measurements of dFe concentration along the U.S. West Coast based on published studies. These
194 include a global compilation (Tagliabue et al., 2016), regional programs such as CalCOFI, CCE-
195 LTER, IRNBRU and MBARI cruises (Bundy et al., 2016; Hogle et al., 2018; Johnson et al., 2003;
196 King and Barbeau, 2011), and additional independent studies (Biller and Bruland, 2013; Boiteau
197 et al., 2019; Bundy et al., 2014, 2015, 2016; Chappell et al., 2019; Chase, 2002; Chase et al., 2005;
198 Firme et al., 2003; Hawco et al., 2021; John et al., 2012; Till et al., 2019). For the final compilation,
199 we define dFe as the sum of the truly dissolved Fe and the dissolvable Fe, following the definitions
200 used in each publication. Different studies used varying filter sizes to define the dFe pool, with
201 0.20, 0.40, and 0.45 μm as the most common. Measurement methods also vary slightly between
202 studies, with samples taken with bottles, pump systems and/or by surface tows. In some cases,
203 samples were acidified for short periods of time before analysis. Despite variable approaches, we
204 find a good agreement between different sets of observations and consider the merged dataset as
205 representative of the dFe distribution in the CCS. The final compilation includes observations from
206 1980 to 2021, with most of the data from the period 1997-2015, and from the upper 100 m of the
207 water column.

208 **2.5 Experimental Design**

209 To evaluate the impact of Fe fluxes from low-oxygen sediment in the SBB on surface
210 biogeochemistry, we designed a suite of model sensitivity experiments with ROMS-BEC in which



211 external sources of Fe are modified relative to a baseline simulation. Accordingly, we run the
212 following model experiments:

213 **Control:** This is the baseline model simulation, using the Fe flux parameterization based on the
214 measurements by (Severmann et al., 2010) following the parameterization by (Deutsch et al.,
215 2021b). Fe release follows the equation:

$$216 \log_{10}\Phi(\text{Fe}) = 2.5 - 0.0165 \cdot \text{O}_2 \text{ (Eq. 1)}$$

217 where O_2 is the concentration of oxygen in mmol m^{-3} and $\Phi(\text{Fe})$ is the Fe flux in $\mu\text{mol m}^{-2} \text{d}^{-1}$.
218 Note that this experiment reflects the original Fe flux parameterization in UCLA's ROMS-BEC
219 and does not include information from the Fe flux measurements conducted during AT42-19,
220 which show significantly higher Fe release under anoxic conditions.

221 **Low Oxygen Threshold:** The purpose of this experiment is to evaluate the importance of enhanced
222 Fe fluxes under low-oxygen conditions in the bottom water. Benthic Fe fluxes are calculated as in
223 *Control*, but capped at a constant value when oxygen decreased below a specific threshold. We
224 performed two “*Low Oxygen Threshold*” model experiments. The first uses an O_2 threshold of 100
225 μM (**Low Oxygen Threshold-100**), and caps Fe release at $0.85 \mu\text{mol m}^{-2} \text{d}^{-1}$ when oxygen drops
226 below $100 \mu\text{M}$. The second uses a threshold of $65 \mu\text{M}$ (**Low Oxygen Threshold-65**), and caps Fe
227 release at $1.48 \mu\text{mol m}^{-2} \text{d}^{-1}$ when oxygen drops below $100 \mu\text{M}$. The $65 \mu\text{M}$ threshold is close to
228 the typical definition of hypoxia ($\sim 60 \mu\text{M}$), while the $100 \mu\text{M}$ threshold was chosen to investigate
229 the general impact of benthic Fe fluxes from low- O_2 coastal sediment, because around 80 % of the
230 shelf in our model is characterized by bottom O_2 concentration lower than $100 \mu\text{M}$ (**Fig. S3**)

231 **High-flux:** This simulation investigates the importance of high benthic Fe fluxes in the SBB, and
232 is based on the new benthic measurements from AT42-19 combined with previous observations
233 (Severmann et al., 2010). We derived and applied a new parameterization for the dependence of
234 benthic Fe flux on bottom O_2 using the combined Fe flux dataset:

$$235 \log_{10}\Phi(\text{Fe}) = 2.86 - 0.01 \cdot \text{O}_2 \text{ (Eq. 2)}$$

236 This revised formulation is only applied in the SBB, while the same formulation as *Control* is used
237 elsewhere. We further corrected a model bias that limits simulations to O_2 concentrations >30



238 mmol m^3 . This correction is crucial to allow the model the estimation of benthic Fe fluxes under
239 anoxic conditions, rather than simulating fluxes at 30 mmol m^3 . We therefore applied a constant
240 deduction of $30 \text{ mmol O}_2 \text{ m}^{-3}$ to the model's bottom water O_2 based on the average difference
241 between model and observed O_2 in the SBB.

242 **Dust-off:** The purpose of this experiment is to evaluate the importance of aeolian Fe deposition in
243 the CCS. In this experiment, the atmospheric Fe deposition is set to zero; all other settings are
244 identical to the *Control* experiment.

245 Each model sensitivity experiment is run separately over a time frame of 6 years from 2004-2009,
246 using the same set of forcings and initial conditions. Results from the final year (2009) are analyzed
247 by comparing differences in biogeochemical fields (Fe, NO_3^- , and NPP) to results from the *Control*
248 run.



249 3. Results

250 3.1 In-situ benthic Fe fluxes and model parameterization

251 Benthic Fe fluxes from in-situ benthic chamber measurements during the AT42-19 expedition are
252 shown in **Table 1**. High Fe flux was recorded at the anoxic depocenter stations (4.90 and 3.92
253 $\text{mmol m}^{-2} \text{d}^{-1}$ at SDRO and 3.49 $\text{mmol m}^{-2} \text{d}^{-1}$ at NDRO). Fe fluxes at the shallower hypoxic
254 stations (NDT3C, NDT3B, and SDT3D) were an order of magnitude lower in comparison. The Fe
255 flux at the hypoxic NDT3A station was approximately half the flux of the depocenter.

256 **Table 1.** Station details and geochemical parameters determined during the AT42-19 expedition. Benthic Fe fluxes
257 were determined using in-situ benthic chambers. Dissolved oxygen concentrations were measured in the water column
258 at 10 m above the seafloor using a Seabird optode sensors attached to the ROV Jason. At stations with two benthic
259 chamber deployments (NDT3A and SDRO), O_2 , coordinates, and depth were averaged as there were only minimal
260 differences between the two chamber deployments.

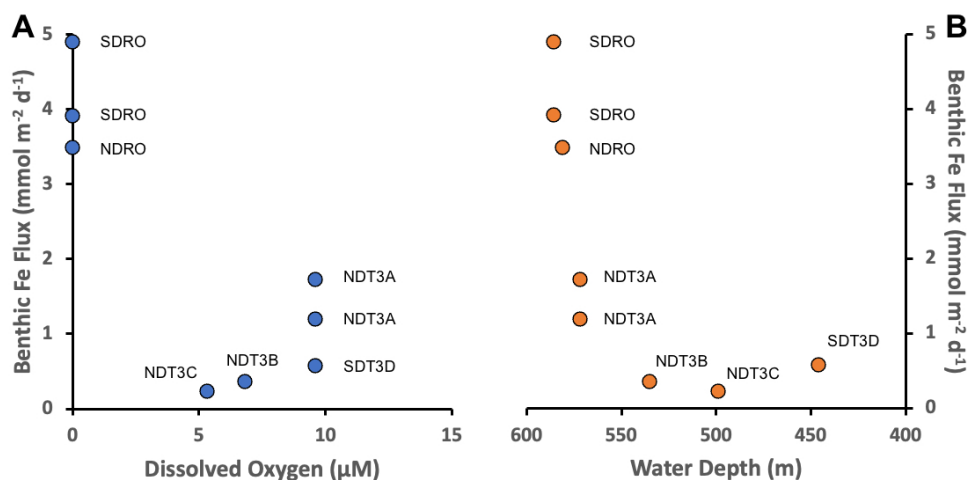
Station	Fe Flux [$\text{mmol m}^{-2} \text{d}^{-1}$]	Oxygen [μM]	Latitude	Longitude	Depth [m]
NDT3C	0.23 (n=1)	5.3	34.3526	-120.0160	499
NDT3B	0.36 (n=1)	6.8	34.3336	-120.0188	535
NDT3A	1.73; 1.20 (n=2)	9.6	34.2921	-120.0258	572
NDRO	3.49 (n=1)	0.0	34.2618	-120.0309	581
SDRO	4.90; 3.92 (n=2)	0.0	34.2011	-120.0446	586
SDT3D	0.58 (n=1)	9.6	34.1422	-120.0515	446

261

262 Trends in the Fe fluxes suggest modulation by oxygen concentration, water depth, and/or
263 bathymetry. We observed a decrease in the Fe flux with a decrease in water depth (**Fig. 2**). There
264 was also a slight trend of higher Fe fluxes with lower O_2 concentrations (most pronounced when
265 oxygen reaches zero); however, since oxygen concentrations were relatively low at all stations
266 ($<10 \mu\text{M}$) it is difficult to distill a clear pattern based on the small dataset. Notably, the NDT3A
267 station showed a high Fe flux despite exhibiting the same oxygen concentration as the shallower
268 station SDT3D. Basin bathymetry may also contribute to observed differences in the flux. For
269 instance, the deeper depocenter and A-station showed higher averaged fluxes than the B, C, and D



270 stations. We further noticed differences between the north and south extension of the transect. The
271 southern stations (SDRO and SDT3D) showed a higher Fe flux than the northern stations (NDRO
272 and NDT3C).



273

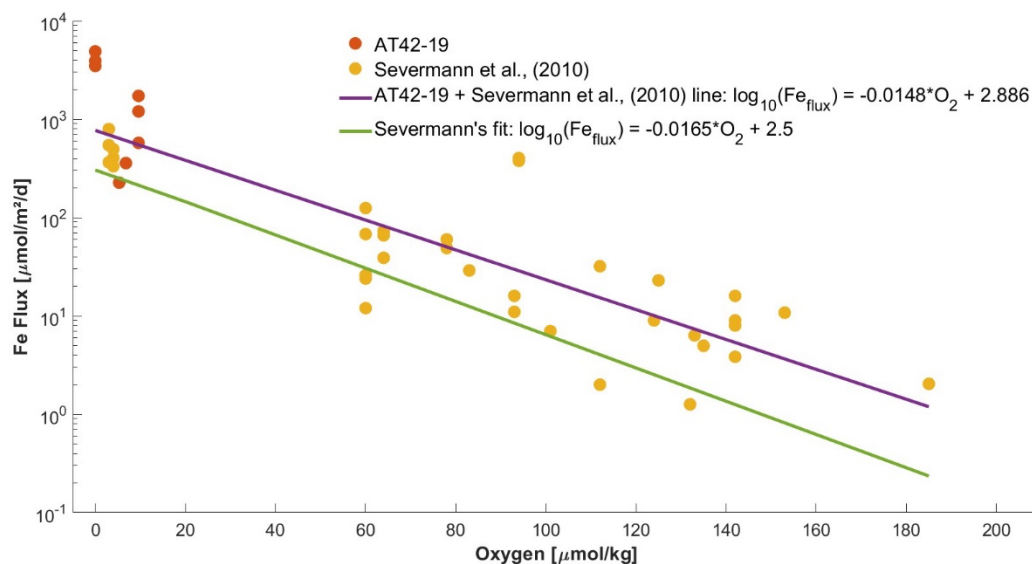
274 **Figure 2.** Benthic in-situ Fe fluxes. A: Fluxes as a function of oxygen. B: Fluxes as a function of
275 (station) water depth. Note that water depth is shown in reverse order. For station details see Table
276 1.

277 We combined Fe fluxes determined during AT42-19 with previous determinations along the CCS,
278 as compiled by (Severmann et al., 2010), and analyzed them as a function of bottom water oxygen
279 (**Fig. 3**). Pooled together, the measurements can be well described by an exponential increase of
280 Fe fluxes with declining bottom water oxygen (Severmann et al., 2010), consistent with the Fe
281 flux parameterization adopted in the ROMS-BEC model (Deutsch et al., 2021b). Several
282 observations from the AT42-19 cruise (red dots in **Fig. 3**) exceed the range of previous
283 measurements (yellow dots in **Fig. 3**), likely owing to the anoxic or near-anoxic conditions in the
284 water. Relative to the exponential fit to the dataset by (Severmann et al., 2010) (green line in **Fig.**
285 **3**) the revised fit to the pooled data (purple line in **Fig. 3**) expands Fe fluxes by approximately two
286 times at oxygen concentrations near zero, and up to one order of magnitude at concentrations near
287 100 μM.



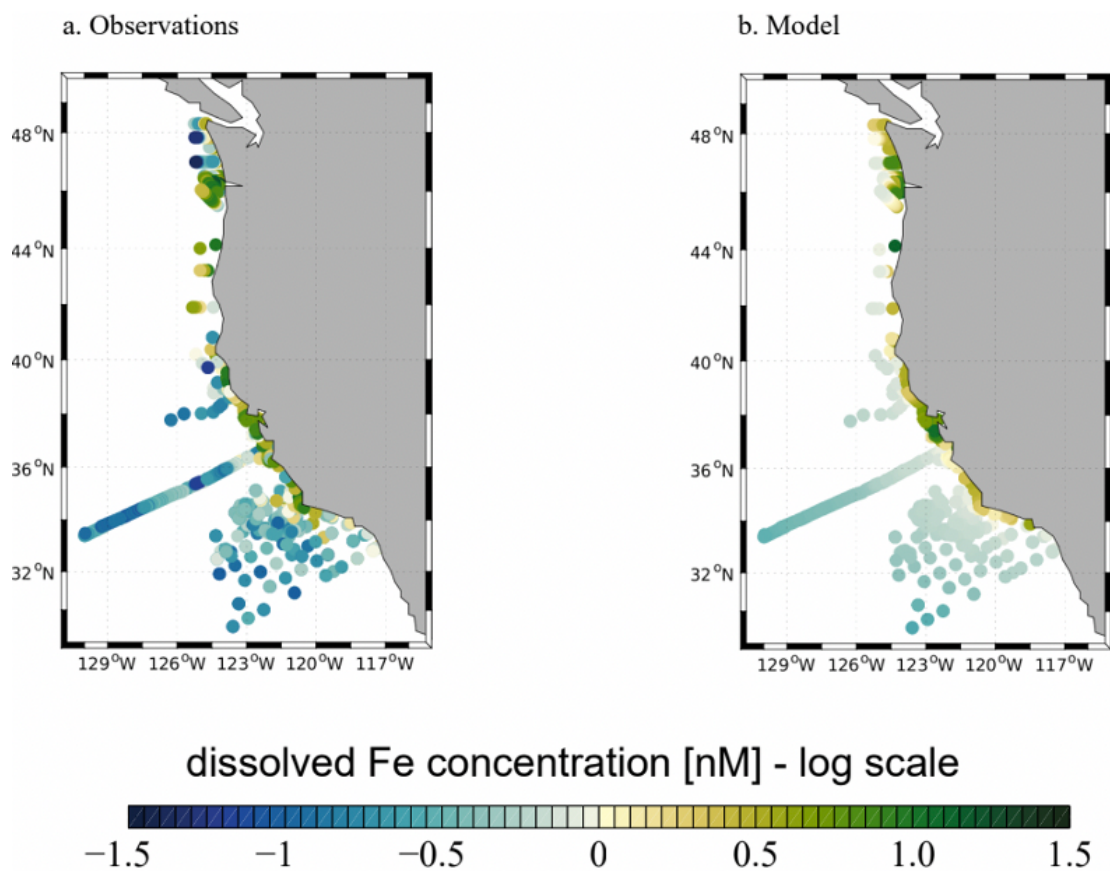
288 3.2 Model evaluation

289 The *Control* simulation captures the magnitude and patterns of the observed dFe distribution in
290 the upper ocean (**Fig. 4**), consistently with our knowledge of the ocean Fe cycle. In both model
291 and observations, dFe concentrations are low at the surface, because of phytoplankton uptake, and
292 increase gradually in subsurface waters due to remineralization and benthic fluxes (**Fig. S4**). The
293 highest dFe concentrations are found along the coast, likely related to high surface productivity
294 and carbon export combined with basin bathymetry and oxygen deficiency. In the open ocean, dFe
295 concentrations are low in both model and observations, reflecting a combination of phytoplankton
296 uptake, scavenging, and low external inputs.



297

298 **Figure 3.** Combined Fe flux data as a function of oxygen. Fe flux data from (Severmann et al.,
299 2010) (orange dots) were fitted with a line of best fit (green) as the original model parametrization.
300 AT42-19 (red dots) were fitted along a line of best fit (purple) that includes Severmann's data
301 point.



302

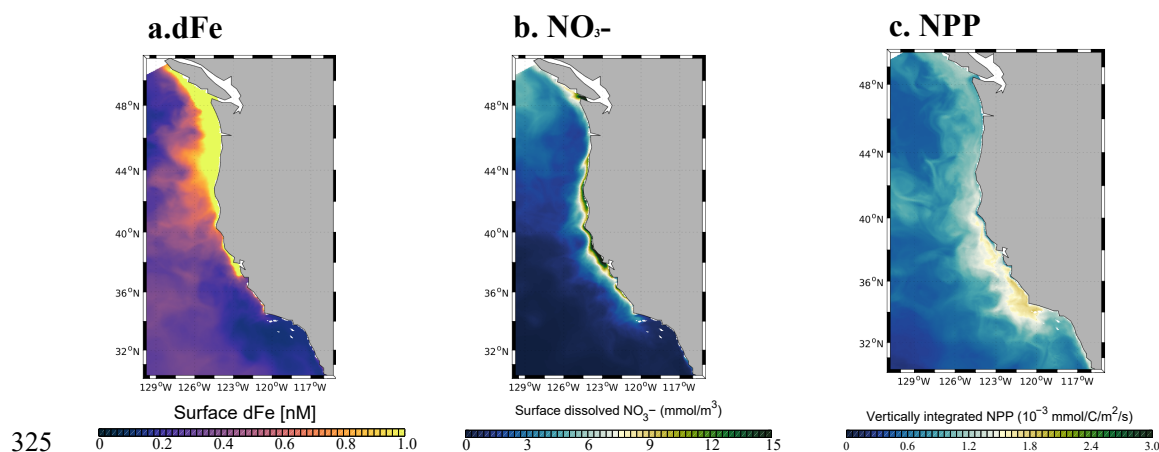
303 **Figure 4.** (a) Observed dFe concentrations (nM) from the U.S. West Coast compilation (see
304 section 2.4) averaged between 0 and 100 m depth. (b) Modeled annual dFe concentrations (nM)
305 averaged between 0 and 100 m depth (note that locations are identical to (a)).

306 The agreement of the model dFe with observations ($R=0.5$, **Fig. 4b**) reflects results from other
307 ocean models compiled in (Tagliabue et al., 2016). However, the model tends to underestimate the
308 sharp dFe gradient between coastal and open ocean waters, overestimating dFe in the open ocean
309 and producing too uniform concentrations offshore and at depth (**Fig. 4; Fig. S4**). These biases are
310 likely related to the simple Fe scavenging scheme, which assumes a constant Fe-binding ligand
311 concentration of 0.6 nM. The low number and episodic nature of in-situ measurements may also
312 explain some of the mismatch between model and observations.



313 At the scale of the CCS, the *Control* simulation produces lower surface dFe in the southern domain
314 (33 - 36°N), and higher surface concentration in the northern domain (40 - 45°N) and near the
315 central coast (**Fig. 5a**). While these patterns reflect a combination of internal Fe cycling and
316 external inputs, the elevated dFe in the northern part of the CCS, in particular offshore, can be
317 partly attributed to higher aeolian deposition in that region (**Fig. S5**) as well as coastal inputs from
318 the Juan De Fuca strait (Deutsch et al., 2021b).

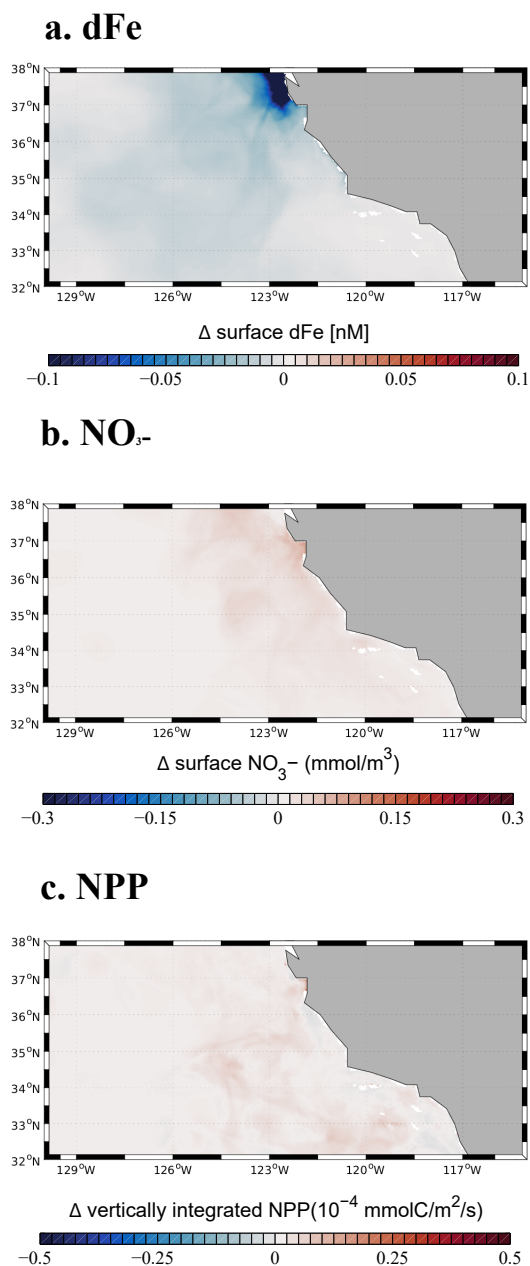
319 Relative to Fe, NO_3^- shows fewer variable patterns along the meridional direction, and a more
320 pronounced signature of coastal upwelling, with higher concentrations nearshore in the central
321 coast (36 – 40°N), and low concentrations in the Southern California Bight and in offshore waters
322 (**Fig. 5b**). The signature of upwelling is also apparent in NPP (**Fig. 5c**), with high values near the
323 coast, in particular in the central region, and decreasing values offshore. These patterns are
324 consistent with observations, as discussed in prior work (Deutsch et al., 2021b)



327 **Fig. 5.** Surface dFe concentration (a), surface NO_3^- concentration (b), and vertically integrated net
328 primary production (NPP) (c) from the *Control* model run.

329 3.3 Low Oxygen Threshold: Impact of benthic Fe flux from low-oxygen bottom water

330 We quantify the importance of benthic Fe fluxes from low-oxygen bottom water by analyzing
331 results from the *Low Oxygen Threshold* experiments, in which we cap the high benthic Fe flux
332 when oxygen declines below a given threshold (**Fig 6**).



333

334

335 **Figure 6.** (a) Surface dFe anomalies, (b) Surface NO₃⁻ anomalies, and (c) vertically integrated net
336 primary production (NPP) from the *Low Oxygen Threshold-100* model run relative to the *Control*
337 model run. Graphs focus on areas around the SBB.



338 As expected, the forced decrease in benthic Fe flux in the *Low Oxygen Threshold-100* simulation
339 leads to a significant decrease in the surface dFe concentration (**Fig. 6a**). This decrease is
340 particularly strong along the coast, but also extends into the open ocean (**Fig S6**). This trend
341 indicates that dFe released from low-oxygen sediment is effectively transported to the surface and
342 offshore, where it can affect primary production. Consistently, the decrease in surface dFe drives
343 a decline in NPP near the coast (**Fig. 6c**), where phytoplankton rely the most on benthic-derived
344 Fe. However, NPP also shows a significant increase offshore, especially between 32N and 36N.
345 This increase can be explained by the relative importance of Fe vs. N limitation along a cross-
346 shore productivity gradient. While near the coast phytoplankton are frequently Fe limited (up to
347 50% of the time in the model), they tend to be almost exclusively N-limited moving offshore
348 (Deutsch et al., 2021b). As Fe limitation reduces NPP near the coast in the *Low Oxygen Threshold-*
349 *100* experiment, NO_3^- utilization also declines, so that more NO_3^- can accumulate in surface waters
350 (**Fig. 6b**). Shallow transport of excess NO_3^- by Ekman transport and eddies can fertilize offshore
351 waters, releasing N limitation and fueling an increase in NPP away from the coast (**Fig. 6c**).

352 In the *Low Oxygen Threshold-65* simulation, the patterns of response are similar to the *Low Oxygen*
353 *Threshold-100* simulation. However, the magnitude of the response is smaller, as only about 50 %
354 of the CCS coast is characterized by bottom O_2 concentrations below 65 μM , as compared to 80
355 % for O_2 below 100 μM . Hence, the decrease in benthic Fe release, and its cascading effects on
356 surface Fe, NO_3^- and NPP are more muted in this simulation (**Fig. S7**).

357 **3.4 High-Flux: Impact of high Fe flux from updated parametrization on NPP, surface dFe,** 358 **and surface NO_3^-**

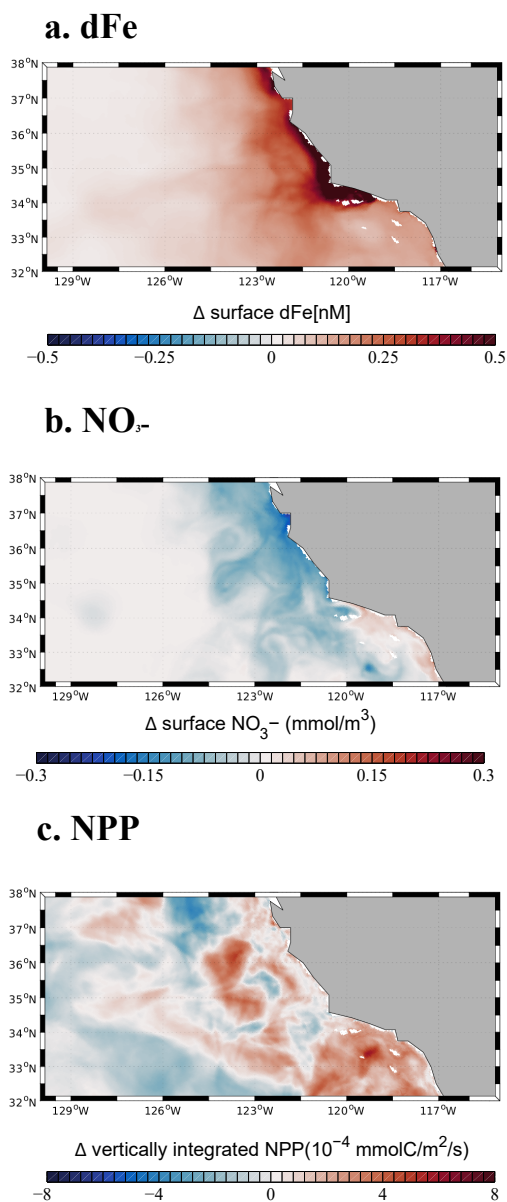
359 The *High-flux* experiment quantifies the impact of the higher benthic Fe fluxes determined during
360 the AT42-19 cruise in the SBB. In this experiment, we observe a dramatic increase of surface dFe
361 along the coast, both within the Santa Barbara Channel, and north of it (**Fig. 7, Fig. S8**). This
362 increase leads to a slight depletion of NO_3^- along the coast (by less than 1 μM), and a patchwork
363 of changes in NPP, with a general increase nearshore and in the southern section of the Southern
364 California Bight, and a decrease offshore. These patterns are opposite in sign to the changes
365 observed in the *Low Oxygen Threshold* experiments, although more intense, and can be explained
366 by similar dynamics. Nearshore, where Fe is more frequently limiting, higher Fe availability



367 releases Fe limitation and drives the higher NPP and more intense NO_3^- drawdown. Further
368 offshore, where waters tend to be more N limited, a reduced supply of NO_3^- decreases NPP.
369 Interestingly, the localized increase in Fe fluxes from the deep SBB has cascading effects on NPP
370 across a much larger region in the CCS. This indicates that Fe released at depth from the anoxic
371 basins is upwelled or mixed to the ocean surface and re-distributed by the oceanic circulation, both
372 northward along the coast, and southward into the Southern California Bight, likely by
373 recirculation within the Southern California Eddy.

374 **3.5 Dust-off: Role of atmospheric Fe deposition**

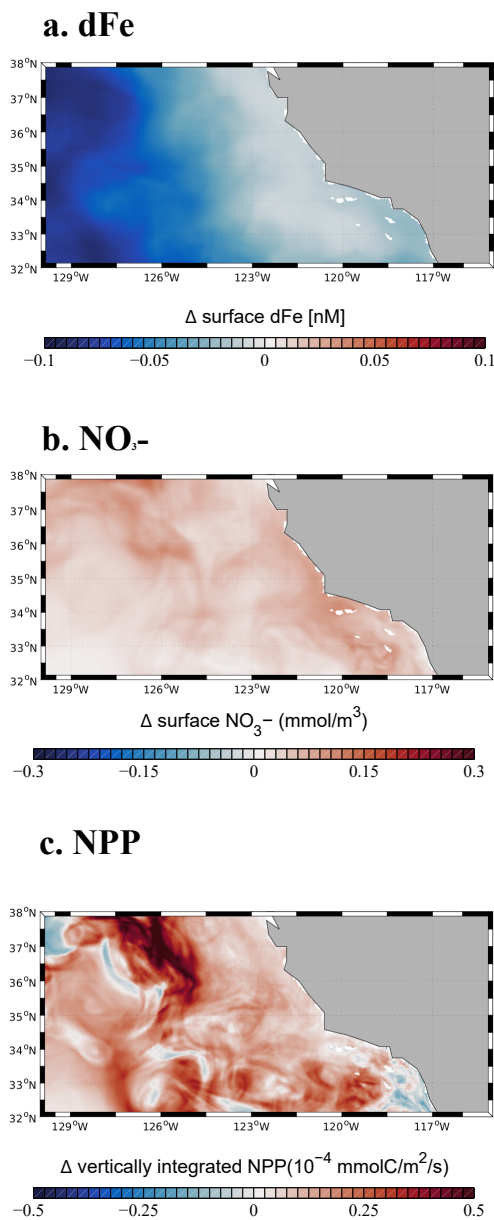
375 We evaluate the importance of aeolian Fe sources in the *Dust-off* simulation, in which atmospheric
376 Fe deposition is set to zero. In this experiment, surface dFe decreases everywhere in the CCS, but
377 the decrease is particularly evident in the open ocean and the northern part of the domain (**Fig. 8a**).
378 This Fe decrease leads to a widespread decrease in NPP in the northern part of the domain (40N
379 to 48N, see **Fig. S9**), with stronger negative anomalies away from the coast. The decline in NPP
380 is accompanied by a broad decrease in NO_3^- utilization, particularly evident offshore, where
381 phytoplankton rely mostly on Fe delivery by dust. In contrast, we observe a broad increase in NPP
382 in the southern part of the domain (south of 40°S) and in coastal areas, likely reflecting increased
383 availability of NO_3^- transported southward by the broad California Current. However, the
384 relatively weak magnitude of NPP responses to changes in dust deposition demonstrate that
385 phytoplankton in the coastal areas and the southern CCS rely more on Fe delivery by benthic
386 sources as compared to atmospheric deposition (**Table S1**).



387

388 **Figure 7.** Surface dFe anomalies (a), Surface NO₃⁻ anomalies (b), and vertically integrated net
389 primary production (NPP) anomalies (c) from the *High-flux* model run relative to the *Control*
390 model run. The graphs focus on areas around the SBB. For the full model domain of the U.S West
391 coast see **Fig. S8**.

392



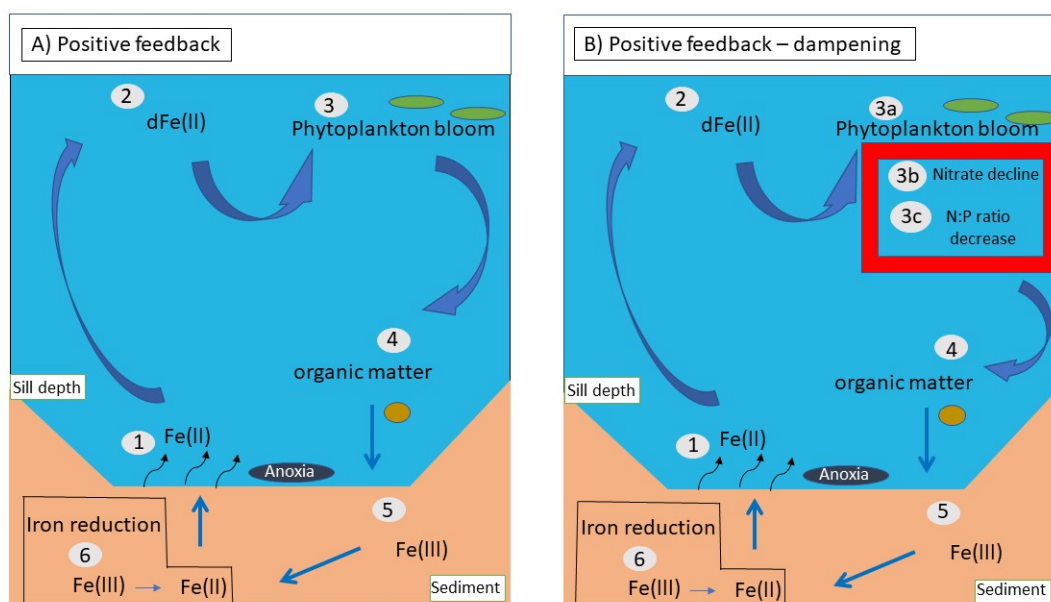
393
394 **Figure 8.** Surface dissolved Fe (a), surface NO₃⁻ anomalies (b), and vertically integrated net
395 primary production (NPP) (c) from the *Dust-off* model run relative to the *Control* model run. The
396 graphs focus on the areas around the SBB. For the full model domain of the U.S West coast see
397 **Fig. S9.**



398 4. Discussion

399 4.1 Benthic Fe flux feedbacks on SBB biogeochemistry

400 The influence of bottom water oxygen concentration on the exchange of solutes between the
401 sediment and the water column has been well documented (Soetaert et al., 2000; Sommer et al.,
402 2016; Testa et al., 2013). Under hypoxic or anoxic bottom water conditions, organic matter
403 sedimentation sustains anaerobic respiration at the sediment-water interface and in the sediment
404 (Furrer and Wehrli, 1993; Middelburg and Levin, 2009). Reduced compounds accumulate in pore
405 waters forming chemical gradients (Widdows and Brinsley, 2002) that result in the flux of solutes
406 such as Fe(II) out of the sediment, and their accumulation in bottom water (Jørgensen and Nelson,
407 2004; McMahon and Chapelle, 1991; Middelburg and Levin, 2009; Yao et al., 2016). Similar
408 conditions are observed in the SBB, where high sedimentation rates, water column denitrification
409 below the sill depth, and high pore-water concentrations of sulfide and Fe(II) have been observed
410 (Behl and Kennett, 1996; Bray et al., 1999; Goericke et al., 2015; Sholkovitz and Soutar, 1975;
411 Sigman et al., 2003; White et al., 2019).



412
413 **Figure 9.** Positive feedback loop in the SBB (A): 1. Benthic Fe release into the anoxic (<3 μM),
414 or severely hypoxic (3-20 μM) bottom water. 2. Upwelled Fe reaches the surface ocean



415 contributing to dFe. 3. Dissolved Fe is assimilated by phytoplankton producing phytoplankton
416 blooms, organic matter and siderophores at the surface. 4. Organic matter is exported from the
417 surface to the deep ocean. 5. Organic matter accumulates at the sediment-water interface. 6. During
418 remineralization of organic matter, iron-reducing bacteria reduce Fe(III) to Fe(II). Negative
419 feedback loop in the SBB (B): 1-3 (not including 3 b and c) and 4-6 are identical to (A). Part 3b
420 and 3c shows the decline of NO_3^- from the amplification of dFe, which causes a decrease in the
421 N:P ratio.

422 The intense flux of dFe from the sediment suggests the potential for positive biogeochemical
423 feedbacks in the SBB and more broadly in the CCS (**Figs. 6 – 8**). However, our simulations also
424 indicate the presence of complex biogeochemical responses between Fe, NO_3^- and NPP that may
425 dampen the effects of these feedbacks.

426 Under a positive feedback scenario (**Fig. 9a**), anoxic and nearly anoxic bottom water conditions
427 facilitate Fe(II) diffusion from the sediment into the bottom water. In the SBB, this Fe eventually
428 reaches the surface via upwelling and mixing processes, which are likely enhanced in the presence
429 of complex bathymetry and islands (Kessouri et al., 2020). This additional dFe input fertilizes
430 coastal waters and increases primary production. Newly formed organic matter eventually sinks
431 towards the seafloor as a rain of organic particles, supporting low-oxygen concentrations in the
432 bottom water, and fueling anaerobic respiration, including Fe reduction, in the sediment. This
433 chain of processes thus represents a positive feedback loop that maintains high Fe(II) release from
434 the sediment, as long as the bottom water remains hypoxic or anoxic (Mills et al., 2004; Noffke et
435 al., 2012; Sañudo-Wilhelmy et al., 2001; Dale et al., 2015). However, our simulations suggest that
436 this positive feedback loop is dampened by increased NO_3^- limitation under higher Fe supply (**Fig.**
437 **9b**), which would limit the increase in NPP. Transport of N-depleted coastal waters reduces NPP
438 offshore (**Fig. 7**), further counteracting the positive feedback loop.

439 Additional processes may dampen or alter this feedback loop. Increased anoxia in bottom water
440 and sediment favors the removal of fixed N by denitrification (Goericke et al., 2015; White et al.,
441 2019). Upwelling of NO_3^- -depleted waters would then reduce surface productivity by increasing
442 N limitation (Gruber and Deutsch, 2014). Release of Fe(II) from the sediment could also impact
443 phosphate dynamics in the SBB. Phosphate is scavenged by iron during oxidation of Fe(II) in the



444 water column and sediment because of the ability of Fe(III) minerals to bind phosphate. After
445 burial, phosphate is released due to reduction of solid Fe(III) minerals to dissolved Fe(II), and
446 diffuses upward to be either re-adsorbed by Fe(III) at the oxic sediment-water interface, or released
447 to the bottom water under anoxic conditions (Dijkstra et al., 2014). The latter scenario is consistent
448 with our in-situ benthic flux chamber measurements revealing increased phosphate releases from
449 the sediment with increased SBB depth (data not shown). Increased release of phosphate into the
450 water column, and transport to the surface, could decrease the N:P ratio of phytoplankton,
451 especially downstream of waters where denitrification occurred (Deutsch et al., 2007). In the
452 presence of N limitation, these conditions could favor the activity of nitrogen-fixing
453 microorganisms (Mills et al., 2004; Noffke et al., 2012; Sañudo-Wilhelmy et al., 2001), further
454 modulating surface NPP (Deutsch et al., 2007).

455 **4.2 Contribution of physical transport on surface Fe**

456 Our numerical experiments suggest that Fe released into the deep SBB can reach and fertilize
457 surface waters. This finding highlights the critical role of bottom water upwelling and mixing in
458 the SBB. There is ample literature describing seasonal surface circulation and bottom water
459 renewal and its effect on nutrients in the SBB (Bray et al., 1999; Hendershott and Winant, 1996;
460 Sholkovitz and Gieskes, 1971). However, the frequency and rate of seasonal bottom water flushing
461 events, and the processes responsible for vertical mixing and upwelling across hundreds of meters
462 remain poorly understood (Shiller et al., 1985; Sholkovitz and Gieskes, 1971; White et al., 2019).
463 It is likely that interaction between wind-driven upwelling events and submesoscale eddies, which
464 are particularly intense inside the Santa Barbara Channel (Kessouri et al., 2020), favors upward
465 mixing of deep bottom water following flushing events.

466 **4.3 Quantifying expansion of anoxia in the SBB**

467 Changes in source waters and global oxygen loss in the Southern California Bight have contributed
468 to decreasing O₂ levels throughout the Southern California Bight and the SBB (Zhou et al., 2022).
469 With the outlook of a continuing decline in oceanic oxygen (Bopp et al., 2013; Kwiatkowski et al.,
470 2020), quantifying the expansion of hypoxic and anoxic zones in the SBB is vital to understand
471 the dynamics and fate of Fe(II) and other reduced compounds (e.g., ammonium (NH₄⁺), hydrogen
472 sulfide (H₂S)) in deep low-oxygen waters. In the SBB, bottom water renewal events have



473 experienced a decline in frequency and magnitude, driving an expansion of hypoxic and anoxic
474 conditions in deep waters (White et al., 2019). This expansion leads to an increase in anaerobic
475 reactions, such as denitrification in the water column (White et al., 2019) as well as Fe reduction,
476 sulfate reduction, and dissimilatory nitrate reduction to ammonium (DNRA) in the sediment
477 (Valentine et al., 2016; Treude et al., 2021; Sommer et al., 2016). Expansion of low oxygen waters
478 could intensify the positive feedback loop between Fe release, NPP and O₂ loss (**Fig. 9**). However,
479 to date, despite the evidence for more frequent anoxia, there is no clear quantitative record of the
480 vertical or horizontal expansions of oxygen-deficient waters in the SBB.



481 5. Conclusion

482 Our field campaign in the SBB measured a remarkably high flux of Fe(II) from the sediment (0.23
483 $-4.9 \text{ mmol m}^{-2} \text{ d}^{-1}$), greater than in previous studies from this region (Severmann et al., 2010) and
484 from other oxygen minimum zones (Dale et al. 2015; Homoky et al. 2021). Using a series of
485 simulations with an ocean biogeochemical model, we show that this high Fe release from deep,
486 low-oxygen sediment has a significant impact on surface nutrients and productivity in the SBB
487 and the Southern California Bight, where Fe is often limiting (Hogle et al., 2018). We also
488 highlight the impacts of coastal Fe inputs on waters further offshore. While phytoplankton in
489 coastal areas directly benefit from Fe fertilization, increased NO_3^- utilization in coastal waters can
490 cause N-limitation of phytoplankton further downstream in open-ocean areas. Thus, benthic Fe
491 fluxes can modulate Fe and NO_3^- limitation in ways that partially counteract one another along the
492 cross-shore productivity gradient of the CCS. Our model simulations also suggest that Fe inputs
493 from atmospheric deposition are mostly important in the open ocean north of 40°N , where
494 phytoplankton rely on Fe delivery by dust. However, we also show that changes in atmospheric
495 Fe deposition can alter ocean productivity in the southern CCS by altering NO_3^- utilization further
496 downstream. Our results support the idea that benthic Fe fluxes are the major source of Fe in the
497 southern CCS and are supplemented by atmospheric deposition in the northwestern region, leading
498 to relatively high NPP coastwide.

499 Over the entire U.S. West Coast, changes in the dependence of benthic Fe release on bottom O_2
500 can halve (*Low Oxygen Threshold-100*) or double (*High-flux*) the mean benthic Fe flux. While our
501 observations are based on snapshots of O_2 and Fe flux, they have implications for the temporal
502 variability of Fe supply. High benthic Fe fluxes are observed during the anoxic fall season, while
503 seasonal flushing in winter and spring likely decrease the flux of Fe by increasing bottom water
504 O_2 and Fe oxidation and retention near the sediment.

505 We suggest that benthic Fe fluxes from deep anoxic basins reach the surface ocean, contributing
506 to feedbacks between Fe and NO_3^- limitation and NPP. Specifically, high Fe fluxes from low-
507 oxygen sediment support higher NPP near the coast, in turn leading to increased respiration and
508 O_2 loss at depth, maintaining high Fe release. This positive feedback loop is dampened by
509 increased NO_3^- limitation, which reduces NPP downstream of coastal regions. This benthic-pelagic



510 coupling demonstrates the importance of sediment-derived Fe fluxes on the coastal ecosystem of
511 the CCS, and the role of vertical transport processes in connecting deep environments to surface
512 waters along continental margins.

513 We highlight the need for further studies focusing on feedbacks between benthic processes and
514 surface biogeochemistry. For example, fixed N loss by denitrification and enhanced release of
515 phosphorous under low-oxygen bottom water are likely to further modulate these interactions.
516 Seasonal studies based on stable isotope, radiotracer, and geochemical techniques are required to
517 track the fate and transport of nutrients in the SBB and similar low-O₂ coastal regions, shedding
518 light on the microbial metabolisms that influences these dynamics. Ocean biogeochemical models
519 for regional and global studies should incorporate new observations of benthic fluxes and their
520 sensitivity to bottom O₂ and other variables. This model adaptation would shed light on the impact
521 of O₂ variability, from seasonal to interannual and longer timescales, including the effects of long-
522 term oceanic O₂ loss, on the feedbacks between benthic nutrient fluxes and surface
523 biogeochemistry.

524



525 **Acknowledgements**

526 We thank the captain and crew of R/V Atlantis, the crew of ROV Jason, the crew of AUV Sentry,
527 and the science party of research cruise AT42-19 for their technical and logistical support. We
528 thank Q. Qin, M. O’Beirne, A. Mazariegos, X. Moreno, and A. Eastman for assisting with
529 shipboard analyses. Funding for this work was provided by the US National Science Foundation,
530 NSF OCE-1829981 (to TT), OCE-1756947 and OCE-1830033 (to DLV), and OCE-2023493 (to
531 DB and ALP). Computational resources were provided by the Expanse system at the San Diego
532 Supercomputer Center through allocation TG-OCE170017 from the Extreme Science and
533 Engineering Discovery Environment (XSEDE), which was supported by National Science
534 Foundation grant 1548562.

535 **Code availability**

536 The physical and biogeochemical codes used for our simulations can be accessed at:
537 <https://github.com/UCLA-ROMS/Code>.

538 The model output can be accessed through Zenodo: (link will be provided before publication)

539

540 **Data availability**

541 In-situ benthic Fe flux data are accessible through the Biological & Chemical Oceanography Data
542 Management Office (BCO-DMO) under the following DOI: (link will be provided before
543 publication).

544 **Author contributions.**

545 DR, TT, DB, and AP conceived this study. DM, DJY, FJ, FW, ECA, KMG, DLV and TT
546 conducted the sampling at sea. DJY transformed and interpreted ROV Jason data. FJ and FW
547 constructed and managed benthic flux chambers. DYJ and DR analyzed Fe(II) and assisted with
548 the flux calculation. MM provided the compiled Fe measurements along the U.S. West Coast. AP
549 and MS performed the model simulations. DR, DB, AP and TT wrote the manuscript with input
550 from all co-authors.

551 **Competing interests**



552 The authors declare that they have no known competing financial interests or personal
553 relationships that could have appeared to influence the work reported in this paper



554 References

- 555 Aumont, O., Ethé, C., Tagliabue, A., Bopp, L., and Gehlen, M.: PISCES-v2: An ocean
556 biogeochemical model for carbon and ecosystem studies, *Geosci. Model Dev.*, 8, 2465–2513,
557 <https://doi.org/10.5194/gmd-8-2465-2015>, 2015.
- 558 Behl, R. J. and Kennett, J. P.: Brief interstadial events in the Santa Barbara basin, NE Pacific,
559 during the past 60 kyr, *Nature*, 379, 243–246, <https://doi.org/10.1038/379243a0>, 1996.
- 560 Biller, D. V. and Bruland, K. W.: Sources and distributions of Mn, Fe, Co, Ni, Cu, Zn, and Cd
561 relative to macronutrients along the central California coast during the spring and summer
562 upwelling season, *Mar. Chem.*, 155, 50–70, <https://doi.org/10.1016/j.marchem.2013.06.003>,
563 2013.
- 564 Boiteau, R. M., Till, C. P., Coale, T. H., Fitzsimmons, J. N., Bruland, K. W., and Repeta, D. J.:
565 Patterns of iron and siderophore distributions across the California Current System, *Limnol.*
566 *Oceanogr.*, 64, 376–389, <https://doi.org/10.1002/lno.11046>, 2019.
- 567 Bopp, L., Resplandy, L., Orr, J. C., Doney, S. C., Dunne, J. P., Gehlen, M., Halloran, P., Heinze,
568 C., Ilyina, T., Séférian, R., Tjiputra, J., and Vichi, M.: Multiple stressors of ocean ecosystems in
569 the 21st century: projections with CMIP5 models, *Biogeosciences*, 10, 6225–6245,
570 <https://doi.org/10.5194/bg-10-6225-2013>, 2013.
- 571 Brander, K., Cochrane, K., Barange, M., and Soto, D.: Climate Change Implications for Fisheries
572 and Aquaculture, in: *Climate Change Impacts on Fisheries and Aquaculture*, edited by: Phillips,
573 B. F. and Pérez-Ramírez, M., John Wiley & Sons, Ltd, Chichester, UK, 45–62,
574 <https://doi.org/10.1002/9781119154051.ch3>, 2017.
- 575 Bray, N. A., Keyes, A., and Morawitz, W. M. L.: The California Current system in the Southern
576 California Bight and the Santa Barbara Channel, *J. Geophys. Res. Oceans*, 104, 7695–7714,
577 <https://doi.org/10.1029/1998JC900038>, 1999.
- 578 Bruland, K. W., Rue, E. L., and Smith, G. J.: Iron and macronutrients in California coastal
579 upwelling regimes: Implications for diatom blooms, *Limnol. Oceanogr.*, 46, 1661–1674,
580 <https://doi.org/10.4319/lo.2001.46.7.1661>, 2001.
- 581 Bruland, K. W., Middag, R., and Lohan, M. C.: Controls of Trace Metals in Seawater, in:
582 *Treatise on Geochemistry*, Elsevier, 19–51, [https://doi.org/10.1016/B978-0-08-095975-7.00602-](https://doi.org/10.1016/B978-0-08-095975-7.00602-1)
583 1, 2014.
- 584 Bundy, R. M., Biller, D. V., Buck, K. N., Bruland, K. W., and Barbeau, K. A.: Distinct pools of
585 dissolved iron-binding ligands in the surface and benthic boundary layer of the California
586 Current, *Limnol. Oceanogr.*, 59, 769–787, <https://doi.org/10.4319/lo.2014.59.3.0769>, 2014.
- 587 Bundy, R. M., Abdulla, H. A. N., Hatcher, P. G., Biller, D. V., Buck, K. N., and Barbeau, K. A.:
588 Iron-binding ligands and humic substances in the San Francisco Bay estuary and estuarine-



- 589 influenced shelf regions of coastal California, *Mar. Chem.*, 173, 183–194,
590 <https://doi.org/10.1016/j.marchem.2014.11.005>, 2015.
- 591 Bundy, R. M., Jiang, M., Carter, M., and Barbeau, K. A.: Iron-Binding Ligands in the Southern
592 California Current System: Mechanistic Studies, *Front. Mar. Sci.*, 3,
593 <https://doi.org/10.3389/fmars.2016.00027>, 2016.
- 594 Capet, X., Campos, E. J., and Paiva, A. M.: Submesoscale activity over the Argentinian shelf,
595 *Geophys. Res. Lett.*, 35, <https://doi.org/10.1029/2008GL034736>, 2008.
- 596 Carr, M.-E. and Kearns, E. J.: Production regimes in four Eastern Boundary Current systems,
597 *Deep Sea Res. Part II Top. Stud. Oceanogr.*, 50, 3199–3221,
598 <https://doi.org/10.1016/j.dsr2.2003.07.015>, 2003.
- 599 Chappell, P., Armbrust, E., Barbeau, K., Bundy, R., Moffett, J., Vedamati, J., and Jenkins, B.:
600 Patterns of diatom diversity correlate with dissolved trace metal concentrations and longitudinal
601 position in the northeast Pacific coastal-offshore transition zone, *Mar. Ecol. Prog. Ser.*, 609, 69–
602 86, <https://doi.org/10.3354/meps12810>, 2019.
- 603 Chase, Z.: Iron, nutrient, and phytoplankton distributions in Oregon coastal waters, *J. Geophys.*
604 *Res.*, 107, 3174, <https://doi.org/10.1029/2001JC000987>, 2002.
- 605 Chase, Z., Johnson, K. S., Elrod, V. A., Plant, J. N., Fitzwater, S. E., Pickell, L., and Sakamoto,
606 C. M.: Manganese and iron distributions off central California influenced by upwelling and shelf
607 width, *Mar. Chem.*, 95, 235–254, <https://doi.org/10.1016/j.marchem.2004.09.006>, 2005.
- 608 Chavez, F. P. and Messié, M.: A comparison of Eastern Boundary Upwelling Ecosystems, *Prog.*
609 *Oceanogr.*, 83, 80–96, <https://doi.org/10.1016/j.pocean.2009.07.032>, 2009.
- 610 Dale, A. W., Nickelsen, L., Scholz, F., Hensen, C., Oeschies, A., and Wallmann, K.: A revised
611 global estimate of dissolved iron fluxes from marine sediments: GLOBAL BENTHIC IRON
612 FLUXES, *Glob. Biogeochem. Cycles*, 29, 691–707, <https://doi.org/10.1002/2014GB005017>,
613 2015.
- 614 Deutsch, C., Sarmiento, J. L., Sigman, D. M., Gruber, N., and Dunne, J. P.: Spatial coupling of
615 nitrogen inputs and losses in the ocean, *Nature*, 445, 163–167,
616 <https://doi.org/10.1038/nature05392>, 2007.
- 617 Deutsch, C., Frenzel, H., McWilliams, J. C., Renault, L., Kessouri, F., Howard, E., Liang, J.-H.,
618 Bianchi, D., and Yang, S.: Biogeochemical variability in the California Current System, *Prog.*
619 *Oceanogr.*, 196, 102565, <https://doi.org/10.1016/j.pocean.2021.102565>, 2021a.
- 620 Deutsch, C., Frenzel, H., McWilliams, J. C., Renault, L., Kessouri, F., Howard, E., Liang, J.-H.,
621 Bianchi, D., and Yang, S.: Biogeochemical variability in the California Current System, *Prog.*
622 *Oceanogr.*, 196, 102565, <https://doi.org/10.1016/j.pocean.2021.102565>, 2021b.



- 623 Dijkstra, N., Kraal, P., Kuypers, M. M. M., Schmetger, B., and Slomp, C. P.: Are Iron-Phosphate
624 Minerals a Sink for Phosphorus in Anoxic Black Sea Sediments?, *PLOS ONE*, 9, e101139,
625 <https://doi.org/10.1371/journal.pone.0101139>, 2014.
- 626 Evans, N., Schroeder, I. D., Pozo Buil, M., Jacox, M. G., and Bograd, S. J.: Drivers of
627 Subsurface Deoxygenation in the Southern California Current System, *Geophys. Res. Lett.*, 47,
628 <https://doi.org/10.1029/2020GL089274>, 2020.
- 629 Firme, G. F., Rue, E. L., Weeks, D. A., Bruland, K. W., and Hutchins, D. A.: Spatial and
630 temporal variability in phytoplankton iron limitation along the California coast and consequences
631 for Si, N, and C biogeochemistry: SPATIAL AND TEMPORAL VARIABILITY IN
632 PHYTOPLANKTON IRON, *Glob. Biogeochem. Cycles*, 17,
633 <https://doi.org/10.1029/2001GB001824>, 2003.
- 634 Furrer, G. and Wehrli, B.: Biogeochemical processes at the sediment-water interface:
635 measurements and modeling, *Appl. Geochem.*, 8, 117–119, [https://doi.org/10.1016/S0883-
636 2927\(09\)80021-8](https://doi.org/10.1016/S0883-2927(09)80021-8), 1993.
- 637 García-Reyes, M. and Largier, J.: Observations of increased wind-driven coastal upwelling off
638 central California, *J. Geophys. Res.*, 115, C04011, <https://doi.org/10.1029/2009JC005576>, 2010.
- 639 Goericke, R., Bograd, S. J., and Grundle, D. S.: Denitrification and flushing of the Santa Barbara
640 Basin bottom waters, *Deep Sea Res. Part II Top. Stud. Oceanogr.*, 112, 53–60,
641 <https://doi.org/10.1016/j.dsr2.2014.07.012>, 2015.
- 642 Grasshoff, K., Kremling, K., and Ehrhardt, M.: *Methods of Seawater Analysis*, 3rd Edn.,
643 Weinheim, Wiley–VCH, 1999.
- 644 Hawco, N. J., Barone, B., Church, M. J., Babcock-Adams, L., Repeta, D. J., Wear, E. K.,
645 Foreman, R. K., Björkman, K. M., Bent, S., Van Mooy, B. A. S., Sheyn, U., DeLong, E. F.,
646 Acker, M., Kelly, R. L., Nelson, A., Ranieri, J., Clemente, T. M., Karl, D. M., and John, S. G.:
647 Iron Depletion in the Deep Chlorophyll Maximum: Mesoscale Eddies as Natural Iron
648 Fertilization Experiments, *Glob. Biogeochem. Cycles*, 35,
649 <https://doi.org/10.1029/2021GB007112>, 2021.
- 650 Hendershott and Winant: Surface Circulation in the Santa Barbara Channel, *Oceanography*, 9,
651 114–121, <https://doi.org/10.5670/oceanog.1996.14>, 1996.
- 652 Hogle, S. L., Dupont, C. L., Hopkinson, B. M., King, A. L., Buck, K. N., Roe, K. L., Stuart, R.
653 K., Allen, A. E., Mann, E. L., Johnson, Z. I., and Barbeau, K. A.: Pervasive iron limitation at
654 subsurface chlorophyll maxima of the California Current, *Proc. Natl. Acad. Sci.*, 115, 13300–
655 13305, <https://doi.org/10.1073/pnas.1813192115>, 2018.
- 656 Homoky, W. B., Conway, T. M., John, S. G., König, D., Deng, F., Tagliabue, A., and Mills, R.
657 A.: Iron colloids dominate sedimentary supply to the ocean interior, *Proc. Natl. Acad. Sci.*, 118,
658 e2016078118, <https://doi.org/10.1073/pnas.2016078118>, 2021.



- 659 John, S. G., Mendez, J., Moffett, J., and Adkins, J.: The flux of iron and iron isotopes from San
660 Pedro Basin sediments, *Geochim. Cosmochim. Acta*, 93, 14–29,
661 <https://doi.org/10.1016/j.gca.2012.06.003>, 2012.
- 662 Johnson, K. S., Elrod, V. A., Fitzwater, S. E., Plant, J. N., Chavez, F. P., Tanner, S. J., Gordon,
663 R. M., Westphal, D. L., Perry, K. D., Wu, J., and Karl, D. M.: Surface ocean-lower atmosphere
664 interactions in the Northeast Pacific Ocean Gyre: Aerosols, iron, and the ecosystem response,
665 *Glob. Biogeochem. Cycles*, 17, <https://doi.org/10.1029/2002GB002004>, 2003.
- 666 Jørgensen, B. B. and Nelson, D. C.: Sulfide oxidation in marine sediments: Geochemistry meets
667 microbiology, in: *Sulfur Biogeochemistry - Past and Present*, Geological Society of America,
668 <https://doi.org/10.1130/0-8137-2379-5.63>, 2004.
- 669 Kessouri, F., Bianchi, D., Renault, L., McWilliams, J. C., Frenzel, H., and Deutsch, C. A.:
670 Submesoscale Currents Modulate the Seasonal Cycle of Nutrients and Productivity in the
671 California Current System, *Glob. Biogeochem. Cycles*, 34, e2020GB006578,
672 <https://doi.org/10.1029/2020GB006578>, 2020.
- 673 King, A. L. and Barbeau, K. A.: Dissolved iron and macronutrient distributions in the southern
674 California Current System, *J. Geophys. Res.*, 116, C03018,
675 <https://doi.org/10.1029/2010JC006324>, 2011.
- 676 Kononets, M., Tengberg, A., Nilsson, M., Ekeröth, N., Hylén, A., Robertson, E. K., van de
677 Velde, S., Bonaglia, S., Rütting, T., Blomqvist, S., and Hall, P. O. J.: In situ incubations with the
678 Gothenburg benthic chamber landers: Applications and quality control, *J. Mar. Syst.*, 214,
679 103475, <https://doi.org/10.1016/j.jmarsys.2020.103475>, 2021.
- 680 Kwiatkowski, L., Torres, O., Bopp, L., Aumont, O., Chamberlain, M., Christian, J. R., Dunne, J.
681 P., Gehlen, M., Ilyina, T., John, J. G., Lenton, A., Li, H., Lovenduski, N. S., Orr, J. C., Palmieri,
682 J., Santana-Falcón, Y., Schwinger, J., Séférian, R., Stock, C. A., Tagliabue, A., Takano, Y.,
683 Tjiputra, J., Toyama, K., Tsujino, H., Watanabe, M., Yamamoto, A., Yool, A., and Ziehn, T.:
684 Twenty-first century ocean warming, acidification, deoxygenation, and upper-ocean nutrient and
685 primary production decline from CMIP6 model projections, *Biogeosciences*, 17, 3439–3470,
686 <https://doi.org/10.5194/bg-17-3439-2020>, 2020.
- 687 Mahowald, N. M., Muhs, D. R., Levis, S., Rasch, P. J., Yoshioka, M., Zender, C. S., and Luo, C.:
688 Change in atmospheric mineral aerosols in response to climate: Last glacial period, preindustrial,
689 modern, and doubled carbon dioxide climates: DUST RESPONSE TO CLIMATE, *J. Geophys.*
690 *Res. Atmospheres*, 111, n/a-n/a, <https://doi.org/10.1029/2005JD006653>, 2006.
- 691 McMahon, P. B. and Chapelle, F. H.: Microbial production of organic acids in aquitard
692 sediments and its role in aquifer geochemistry, *Nature*, 349, 233–235,
693 <https://doi.org/10.1038/349233a0>, 1991.
- 694 Middelburg, J. J. and Levin, L. A.: Coastal hypoxia and sediment biogeochemistry,
695 *Biogeosciences*, 6, 1273–1293, <https://doi.org/10.5194/bg-6-1273-2009>, 2009a.



- 696 Mills, M. M., Ridame, C., Davey, M., La Roche, J., and Geider, R. J.: Iron and phosphorus co-
697 limit nitrogen fixation in the eastern tropical North Atlantic, *Nature*, 429, 292–294,
698 <https://doi.org/10.1038/nature02550>, 2004.
- 699 Moore, J. K. and Braucher, O.: Sedimentary and mineral dust sources of dissolved iron to the
700 world ocean, *Biogeosciences*, 5, 631–656, <https://doi.org/10.5194/bg-5-631>, 2008.
- 701 Moore, J. K., Doney, S. C., Kleypas, J. A., Glover, D. M., and Fung, I. Y.: An intermediate
702 complexity marine ecosystem model for the global domain, *Deep Sea Res. Part II Top. Stud.*
703 *Oceanogr.*, 49, 403–462, [https://doi.org/10.1016/S0967-0645\(01\)00108-4](https://doi.org/10.1016/S0967-0645(01)00108-4), 2001.
- 704 Moore, J. K., Doney, S. C., and Lindsay, K.: Upper ocean ecosystem dynamics and iron cycling
705 in a global three-dimensional model: GLOBAL ECOSYSTEM-BIOGEOCHEMICAL MODEL,
706 *Glob. Biogeochem. Cycles*, 18, n/a-n/a, <https://doi.org/10.1029/2004GB002220>, 2004.
- 707 Noffke, A., Hensen, C., Sommer, S., Scholz, F., Bohlen, L., Mosch, T., Graco, M., and
708 Wallmann, K.: Benthic iron and phosphorus fluxes across the Peruvian oxygen minimum zone,
709 *Limnol. Oceanogr.*, 57, 851–867, <https://doi.org/10.4319/lo.2012.57.3.0851>, 2012.
- 710 Pham, A. L. D. and Ito, T.: Formation and Maintenance of the GEOTRACES Subsurface-
711 Dissolved Iron Maxima in an Ocean Biogeochemistry Model, *Glob. Biogeochem. Cycles*, 32,
712 932–953, <https://doi.org/10.1029/2017GB005852>, 2018.
- 713 Pham, A. L. D. and Ito, T.: Ligand Binding Strength Explains the Distribution of Iron in the
714 North Atlantic Ocean, *Geophys. Res. Lett.*, 46, 7500–7508,
715 <https://doi.org/10.1029/2019GL083319>, 2019.
- 716 Pozo Buil, M. and Di Lorenzo, E.: Decadal dynamics and predictability of oxygen and
717 subsurface tracers in the California Current System, *Geophys. Res. Lett.*, 44, 4204–4213,
718 <https://doi.org/10.1002/2017GL072931>, 2017.
- 719 Reimers, C. E., Lange, C. B., Tabak, M., and Bernhard, J. M.: Seasonal spillover and varve
720 formation in the Santa Barbara Basin, California, *Limnol. Oceanogr.*, 35, 1577–1585,
721 <https://doi.org/10.4319/lo.1990.35.7.1577>, 1990.
- 722 Renault, L., Deutsch, C., McWilliams, J. C., Frenzel, H., Liang, J.-H., and Colas, F.: Partial
723 decoupling of primary productivity from upwelling in the California Current system, *Nat.*
724 *Geosci.*, 9, 505–508, <https://doi.org/10.1038/ngeo2722>, 2016.
- 725 Renault, L., McWilliams, J. C., Kessouri, F., Jousse, A., Frenzel, H., Chen, R., and Deutsch, C.:
726 Evaluation of high-resolution atmospheric and oceanic simulations of the California Current
727 System, *Prog. Oceanogr.*, 195, 102564, <https://doi.org/10.1016/j.pocean.2021.102564>, 2021.
- 728 Sañudo-Wilhelmy, S., Kustka, A., Gobler, C., Hutchins, D., Yang, M., Lwiza, K., Burns, J.,
729 Raven, J., and Carpenter, E.: Phosphorus limitation of nitrogen fixation by *Trichodesmium* in the
730 central Atlantic Ocean, *Nature*, 411, 66–9, <https://doi.org/10.1038/35075041>, 2001.



- 731 Severmann, S., McManus, J., Berelson, W. M., and Hammond, D. E.: The continental shelf
732 benthic iron flux and its isotope composition, *Geochim. Cosmochim. Acta*, 74, 3984–4004,
733 <https://doi.org/10.1016/j.gca.2010.04.022>, 2010.
- 734 Shchepetkin, A. F.: An adaptive, Courant-number-dependent implicit scheme for vertical
735 advection in oceanic modeling, *Ocean Model.*, 91, 38–69,
736 <https://doi.org/10.1016/j.ocemod.2015.03.006>, 2015.
- 737 Shchepetkin, A. F. and McWilliams, J. C.: The regional oceanic modeling system (ROMS): a
738 split-explicit, free-surface, topography-following-coordinate oceanic model, *Ocean Model.*, 9,
739 347–404, <https://doi.org/10.1016/j.ocemod.2004.08.002>, 2005.
- 740 Shiller, A. M., Gieskes, J. M., and Brian Price, N.: Particulate iron and manganese in the Santa
741 Barbara Basin, California, *Geochim. Cosmochim. Acta*, 49, 1239–1249,
742 [https://doi.org/10.1016/0016-7037\(85\)90013-4](https://doi.org/10.1016/0016-7037(85)90013-4), 1985.
- 743 Sholkovitz, E. and Soutar, A.: Changes in the composition of the bottom water of the Santa
744 Barbara Basin: effect of turbidity currents, *Deep Sea Res. Oceanogr. Abstr.*, 22, 13–21,
745 [https://doi.org/10.1016/0011-7471\(75\)90014-5](https://doi.org/10.1016/0011-7471(75)90014-5), 1975.
- 746 Sholkovitz, E. R. and Gieskes, J. M.: A PHYSICAL-CHEMICAL STUDY OF THE FLUSHING
747 OF THE SANTA BARBARA BASIN1: FLUSHING OF THE SANTA BARBARA BASIN,
748 *Limnol. Oceanogr.*, 16, 479–489, <https://doi.org/10.4319/lo.1971.16.3.0479>, 1971.
- 749 Sigman, D. M., Robinson, R., Knapp, A. N., van Geen, A., McCorkle, D. C., Brandes, J. A., and
750 Thunell, R. C.: Distinguishing between water column and sedimentary denitrification in the
751 Santa Barbara Basin using the stable isotopes of nitrate, *Geochem. Geophys. Geosystems*, 4,
752 <https://doi.org/10.1029/2002GC000384>, 2003.
- 753 Soetaert, K., Middelburg, J. J., Herman, P. M. J., and Buis, K.: On the coupling of benthic and
754 pelagic biogeochemical models, *Earth-Sci. Rev.*, 51, 173–201, [https://doi.org/10.1016/S0012-8252\(00\)00004-0](https://doi.org/10.1016/S0012-8252(00)00004-0), 2000.
- 756 Sommer, S., Gier, J., Treude, T., Lomnitz, U., Dengler, M., Cardich, J., and Dale, A. W.:
757 Depletion of oxygen, nitrate and nitrite in the Peruvian oxygen minimum zone cause an
758 imbalance of benthic nitrogen fluxes, *Deep Sea Res. Part I*, 112, 113–122,
759 <https://doi.org/10.1016/j.dsr.2016.03.001>, 2016.
- 760 Tagliabue, A., Sallée, J.-B., Bowie, A. R., Lévy, M., Swart, S., and Boyd, P. W.: Surface-water
761 iron supplies in the Southern Ocean sustained by deep winter mixing, *Nat. Geosci.*, 7, 314–320,
762 <https://doi.org/10.1038/ngeo2101>, 2014.
- 763 Tagliabue, A., Aumont, O., DeAth, R., Dunne, J. P., Dutkiewicz, S., Galbraith, E., Misumi, K.,
764 Moore, J. K., Ridgwell, A., Sherman, E., Stock, C., Vichi, M., Völker, C., and Yool, A.: How
765 well do global ocean biogeochemistry models simulate dissolved iron distributions?: GLOBAL
766 IRON MODELS, *Glob. Biogeochem. Cycles*, 30, 149–174,
767 <https://doi.org/10.1002/2015GB005289>, 2016.



- 768 Tagliabue, A., Bowie, A. R., Boyd, P. W., Buck, K. N., Johnson, K. S., and Saito, M. A.: The
769 integral role of iron in ocean biogeochemistry, *Nature*, 543, 51–59,
770 <https://doi.org/10.1038/nature21058>, 2017.
- 771 Testa, J. M., Brady, D. C., Di Toro, D. M., Boynton, W. R., Cornwell, J. C., and Kemp, W. M.:
772 Sediment flux modeling: Simulating nitrogen, phosphorus, and silica cycles, *Estuar. Coast. Shelf*
773 *Sci.*, 131, 245–263, <https://doi.org/10.1016/j.ecss.2013.06.014>, 2013.
- 774 Till, C. P., Solomon, J. R., Cohen, N. R., Lampe, R. H., Marchetti, A., Coale, T. H., and Bruland,
775 K. W.: The iron limitation mosaic in the California Current System: Factors governing Fe
776 availability in the shelf/near-shelf region, *Limnol. Oceanogr.*, 64, 109–123,
777 <https://doi.org/10.1002/lno.11022>, 2019.
- 778 Treude, T., Smith, C. R., Wenzhöfer, F., Carney, E., Bernardino, A. F., Hannides, A. K., Krüger,
779 M., and Boetius, A.: Biogeochemistry of a deep-sea whale fall: sulfate reduction, sulfide efflux
780 and methanogenesis, *Mar. Ecol. Prog. Ser.*, 382, 1–21, 2009.
- 781 Treude, T., Hamdan, L. J., Lemieux, S., Dale, A. W., and Sommer, S.: Rapid sulfur cycling in
782 sediments from the Peruvian oxygen minimum zone featuring simultaneous sulfate reduction and
783 sulfide oxidation, *Limnol. Oceanogr.*, 66, 2661–2671, <https://doi.org/10.1002/lno.11779>, 2021.
- 784 Valentine, D. L., Fisher, G. B., Pizarro, O., Kaiser, C. L., Yoerger, D., Breier, J. A., and Tarn, J.:
785 Autonomous Marine Robotic Technology Reveals an Expansive Benthic Bacterial Community
786 Relevant to Regional Nitrogen Biogeochemistry, *Environ. Sci. Technol.*, 50, 11057–11065,
787 <https://doi.org/10.1021/acs.est.6b03584>, 2016.
- 788 White, M. E., Rafter, P. A., Stephens, B. M., Wankel, S. D., and Aluwihare, L. I.: Recent
789 Increases in Water Column Denitrification in the Seasonally Suboxic Bottom Waters of the
790 Santa Barbara Basin, *Geophys. Res. Lett.*, 46, 6786–6795,
791 <https://doi.org/10.1029/2019GL082075>, 2019.
- 792 Widdows, J. and Brinsley, M.: Impact of biotic and abiotic processes on sediment dynamics and
793 the consequences to the structure and functioning of the intertidal zone, *J. Sea Res.*, 48, 143–156,
794 [https://doi.org/10.1016/S1385-1101\(02\)00148-X](https://doi.org/10.1016/S1385-1101(02)00148-X), 2002.
- 795 Yao, M., Henny, C., and Maresca, J. A.: Freshwater Bacteria Release Methane as a By-Product
796 of Phosphorus Acquisition, *Appl. Environ. Microbiol.*, 82, 6994–7003,
797 <https://doi.org/10.1128/AEM.02399-16>, 2016.
- 798 Zhou, Y., Gong, H., and Zhou, F.: Responses of Horizontally Expanding Oceanic Oxygen
799 Minimum Zones to Climate Change Based on Observations, *Geophys. Res. Lett.*, 49,
800 [e2022GL097724](https://doi.org/10.1029/2022GL097724), <https://doi.org/10.1029/2022GL097724>, 2022.

801